

# Holographic Measurements of Anisotropic Three-Dimensional Diffusion of Colloidal Clusters

Jerome Fung

*Department of Physics, Harvard University,  
Cambridge, Massachusetts 02138, USA*

Vinothan N. Manoharan\*

*School of Engineering and Applied Sciences,  
Harvard University, Cambridge, Massachusetts 02138, USA and  
Department of Physics, Harvard University,  
Cambridge, Massachusetts 02138, USA*

(Dated: May 8, 2013)

## Abstract

We use digital holographic microscopy to measure the three-dimensional (3D) diffusion tensor  $\mathbf{D}$  for clusters of colloidal spheres, including both dimers and triangular trimers of spheres, for which no analytical calculation of the diffusion tensor exists. We measure all nonzero elements of the diffusion tensor to a precision of 1% or better, and we detect anisotropic rotational and translational diffusion arising from the asymmetries of the clusters. In the case of the three-particle triangular cluster, we also detect a small but statistically significant difference in the rotational diffusion about the two in-plane axes. We attribute this difference to weak breaking of threefold rotational symmetry due to a small amount of particle polydispersity. Our experimental measurements agree well with theoretical predictions and show how diffusion constants can be measured under conditions relevant to colloidal self-assembly, where theoretical and even numerical prediction is difficult.

Diffusion plays a critical role in the dynamics, self-assembly, and rheology of complex fluids. In systems such as colloidal suspensions, which typically have short-ranged interaction potentials, diffusion can in fact play a larger role than energy barriers in setting transition rates [1]. However, the diffusion of geometrically anisotropic particles, a common class of colloidal suspension that can also arise as intermediates in the self-assembly of spherical particles, can be difficult to predict. Theoretically determining friction factors for these particles requires analytically solving Stokes' equation, which is only possible for highly symmetric particles such as ellipsoids [2] or sphere dimers [3] in unbounded fluids. Numerical methods such as bead modeling [4] or finite-element methods [5–7] require approximating the shape of the particles or the hydrodynamic interactions. These methods are difficult to apply when asymmetric particles diffuse near rigid boundaries or other particles, two situations that are relevant to colloidal self-assembly and dynamics in general. Thus experimental measurements of diffusion tensors are crucial.

In particular, measurements on single particles rather than ensembles are necessary. Anisotropic particles show multiple diffusion timescales that are difficult to resolve through bulk techniques such as depolarized dynamic light scattering [8]. Existing techniques for measuring single-particle diffusion are also difficult to apply in 3D. Video microscopy, for example, has been used to measure two-dimensional (2D) diffusion of colloidal ellipsoids [9, 10] and planar sphere clusters [11] but yields limited information about out-of-plane motions [12–14]. Confocal microscopy can be used to study the 3D Brownian dynamics of a range of geometrically anisotropic particles [15, 16], but can take on the order of 1 s to acquire a 3D stack. This can make it challenging to probe timescales comparable to particle diffusion times or to study rare processes such as the early stages of self-assembly [17].

In this Letter, we present precise measurements of 3D diffusion tensors of individual colloidal clusters using a fast 3D imaging technique, in-line digital holographic microscopy (DHM). In DHM one records a 2D hologram generated by interference between light scattered from colloidal particles and the undiffracted, transmitted beam (Fig. 1(a)). The 2D holograms can be acquired much more rapidly than 3D confocal stacks. By fitting models based on electromagnetic scattering solutions [18–20], we recover the 3D dynamics of dimers and triangular trimers of colloidal spheres. We resolve all the translational and rotational components of the diffusion tensor and detect the asymmetries of these clusters. We also show that a small amount of polydispersity leads to symmetry breaking in the rotational

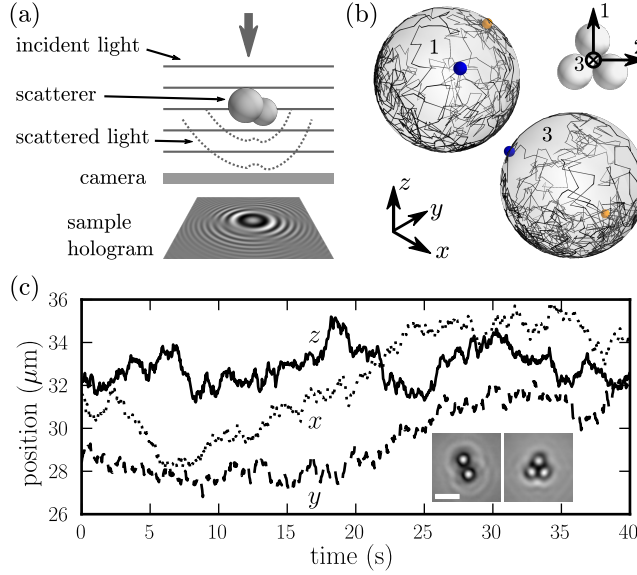


FIG. 1. (Color online) (a) Schematic overview of in-line holographic microscope used in the experiments. (b) Axis trajectories for a diffusing triangular cluster of 1  $\mu\text{m}$  diameter polystyrene spheres (inset: orientation of cluster axes). Renderings show the trajectories of axes 1 and 3 on a unit sphere. Blue (dark) markers indicate the start of the 40 s trajectory and Orange (light) markers the end. (c) Laboratory-frame center-of-mass trajectories of the same triangular cluster over the same time interval as in (b). Inset: amplitude reconstructions [21] of the holograms, showing the structure of the measured clusters. Scale bar, 2  $\mu\text{m}$ .

diffusion components. Our measurements agree well with numerical predictions and, more generally, show how diffusion tensors can be measured in experimental systems relevant to self-assembly, where theoretical predictions are challenging.

The diffusion tensor  $\mathbf{D}$  quantifies the translational and rotational Brownian diffusion of an arbitrary rigid colloidal particle. In general, six generalized coordinates  $q^i$  (three positions and three orientation angles) are needed to describe the position and orientation of a rigid body. Although  $\mathbf{D}$  is rigorously defined by generalizing Fick's law to an abstract ensemble of particles diffusing in this 6-dimensional configuration space,  $\mathbf{D}$  also describes correlations between displacements of the  $q^i$  for short lag times  $\tau$  [22, 23][24]:

$$\langle \Delta q^i \Delta q^j \rangle = 2D^{ij}\tau. \quad (1)$$

$\mathbf{D}$  may be partitioned into the following  $3 \times 3$  blocks:

$$\mathbf{D} = \begin{pmatrix} \mathbf{D}^{tt} & \mathbf{D}^{tr} \\ \mathbf{D}^{tr} & \mathbf{D}^{rr} \end{pmatrix}. \quad (2)$$

$\mathbf{D}^{tt}$  describes translational diffusion,  $\mathbf{D}^{rr}$  rotational diffusion, and  $\mathbf{D}^{tr}$  translation-rotation coupling. The generalized Stokes-Einstein equation relates  $\mathbf{D}$  to the friction tensor  $\mathfrak{F}$  describing the hydrodynamic Stokes drag forces and torques on a moving particle:  $\mathbf{D} = k_B T \mathfrak{F}^{-1}$  [22, 23]. Predicting  $\mathbf{D}$  thus requires a solution for the Stokes flow around a particle. Dimers are one of the few non-spherical shapes for which analytical solutions exist; none exist for trimers.

We make dimer and triangular trimer clusters through limited aggregation of sulfate polystyrene spheres (Invitrogen) [25], 1.3- $\mu\text{m}$  diameter for dimers and 1- $\mu\text{m}$  diameter for trimers. We transfer these particles into a 250 mM NaCl solution to screen the charge of the stabilizing sulfate groups and start the aggregation, then we decrease the ionic strength by quenching with deionized water (Millipore) after 1 minute to arrest the aggregation. We then suspend the resulting mixture of single particles, dimers, and larger clusters in a density-matched solvent consisting of 50% v/v  $\text{D}_2\text{O}$  and 50% v/v  $\text{H}_2\text{O}$  with a salt concentration of 1 mM. We load the particles into sample cells made from glass slides, coverslips, and 76- $\mu\text{m}$  thick Mylar spacers [19, 20]. After finding a cluster with the desired morphology using bright field microscopy, we ensure that it is at least 30  $\mu\text{m}$  away from sample cell walls or other particles so that the cluster diffusion is unhindered by boundaries [26]. We record holograms using an instrument previously described in the literature [17, 20] at a frame rate of 25 frames per second and a temperature  $T = 296 \pm 2$  K.

We then analyze the measured holograms to obtain 3D trajectories of the clusters. We obtain particle sizes, refractive indices, center-of-mass 3D positions, and three orientation angles (two for dimers) by fitting an exact scattering solution to Maxwell's equations to each recorded hologram [19, 27][28]. Figs. 1(b) and (c) show some of the 3D data we obtain for a trimer. We measure the components of the translational block  $\mathbf{D}^{tt}$  by directly applying Eq. 1, where the relevant  $\Delta q^i$  are relative to a coordinate system rigidly fixed to the cluster [19, 22, 23]. The correlation functions needed to measure the diagonal components of  $\mathbf{D}^{tt}$  are cluster-frame mean-squared displacements (MSDs). To measure the components of  $\mathbf{D}^{rr}$ , we examine the dynamics of the axis vectors  $\mathbf{u}_i$  fixed to a cluster. The tips of the  $\mathbf{u}_i$  diffuse along the surface of a unit sphere, as illustrated in Fig. 1(b). We compute

autocorrelations of the  $\mathbf{u}_i$ , which are related to  $D_{r,i}$ , the 3 diagonal components of  $\mathbf{D}^{rr}$ , as follows [29]:

$$\langle \mathbf{u}_i(t) \cdot \mathbf{u}_i(t + \tau) \rangle = \exp \left[ \left( D_{r,i} - \sum_j D_{r,j} \right) \tau \right]. \quad (3)$$

For the axisymmetric dimer, we consider a related quantity, the MSD of the axis unit vector  $\mathbf{u}$  [15, 19, 30, 31]:

$$\langle \Delta \mathbf{u}^2(\tau) \rangle = 2(1 - \langle \mathbf{u}(t) \cdot \mathbf{u}(t + \tau) \rangle). \quad (4)$$

We find good agreement between  $\mathbf{D}$  for a dimer, measured to 0.5% precision from a time series of 22,000 holograms, and analytical and numerical predictions. The measured axis MSD, along with a best fit to Eq. 4, and the cluster-frame MSDs are shown in Fig. 2. Dimers of two identical spheres have three mirror planes and an axis of continuous rotational symmetry, so in the coordinate system shown in the inset of Fig. 2(b),  $\mathbf{D}$  is diagonal. But due to the breaking of spherical symmetry,  $\mathbf{D}$  has four rather than two unique elements: the translational diffusion constants  $D_{\parallel}$  and  $D_{\perp}$ , and the rotational diffusion constants  $D_{r,\parallel}$  and  $D_{r,\perp}$ , where the subscripts denote motions parallel to and perpendicular to the dimer axis [19, 22]. Because we cannot observe rotations about the dimer axis, we can only measure  $D_{r,\perp}$ . Moreover, we can only measure a combined MSD,  $\langle \Delta x_{\perp}(\tau)^2 \rangle$ , representing translation along the two degenerate perpendicular axes. We then extract  $D_{\parallel}$  and  $D_{\perp}$  from linear fits to the MSDs.  $\langle \Delta x_{\parallel}^2(\tau) \rangle$  has a slope of  $2D_{\parallel}$  in accordance with Eq. 1, and  $\langle \Delta x_{\perp}^2(\tau) \rangle$  has a slope of  $4D_{\perp}$ . Our measurement of  $D_{\parallel}/D_{\perp}$ , which is a universal constant for any Brownian dimer, agrees well with predictions from the shell modeling code HYDROSUB [32] and the exact Stokes solution of Nir & Acrivos [3] (Table I).

The individual elements of  $\mathbf{D}$  also agree with calculations, once we account for the sphere radius  $a$  and the solvent viscosity  $\eta$ . We determine an effective sphere radius  $a_{\text{eff}}$  from the measured ratios  $D_{\parallel}/D_{r,\perp}$  and  $D_{\perp}/D_{r,\perp}$ , which depend only on  $a$  [3]. Then we determine the best-fit  $\eta_{\text{eff}}$  from the measured elements of  $\mathbf{D}$ . We find an effective  $a_{\text{eff}} = 709$  nm, which is larger than the optical radius  $a_{\text{opt}} = 650$  nm obtained from DHM. The larger effective radius is consistent with typical dynamic light scattering measurements of the size of colloidal spheres, which show enhanced hydrodynamic radii due to charge or hairy surface layers on the particles [34, 35]. The best-fit viscosity is  $\eta_{\text{eff}} = 1.159$  mPa s, consistent with measurements of the diffusion constant of a freely diffusing sphere in the same sample, which acts as an *in situ* thermometer, combined with bulk viscosity measurements using a Cannon-

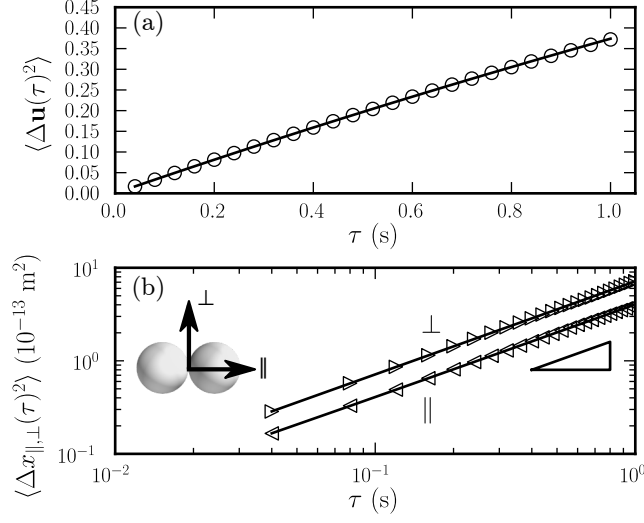


FIG. 2. (a) Axis MSD for dimer of 1.3- $\mu\text{m}$  diameter spheres. Open symbols are measurements; solid line is the best-fit to Eq. 4, where  $\langle \mathbf{u}(t) \cdot \mathbf{u}(t + \tau) \rangle = \exp(-2D_{r,\perp}\tau)$ . (b) Cluster-frame MSD computed for the same dimer as in (a). Open symbols are measurements; solid lines are linear fits. Triangle shows slope of 1. Error bars are calculated using a block decorrelation technique [33]; they are comparable in size to the plotting symbols or smaller. Inset: orientation of parallel ( $\parallel$ ) and perpendicular ( $\perp$ ) axes.

Manning capillary viscometer; these together give a solvent viscosity of  $1.19 \pm 0.04$  mPa.s. We use this procedure because the solvent viscosity has a strong temperature dependence [28]. The elements of  $\mathbf{D}$  computed with these effective parameters agree with our measurements to better than 1% (Table I). We also note that the HYDROSUB prediction for  $D_{r,\perp}$  differs from the analytical prediction by about 1%, which is consistent with prior studies [4]. The agreement between our measurements and the analytical prediction suggests that our measurement accuracy is at least comparable to, if not better than, that of HYDROSUB.

Measurements on trimers reveal anisotropic translational and rotational diffusion. Trimers of identical particles have two mirror planes, making  $\mathbf{D}^{tt}$  and  $\mathbf{D}^{rr}$  diagonal [22, 36] in the coordinate system shown in the inset of Fig. 1b. We denote the six diagonal elements as  $D_{t,1}$ ,  $D_{t,2}$ ,  $D_{t,3}$ ,  $D_{r,1}$ ,  $D_{r,2}$ , and  $D_{r,3}$ . In contrast to dimers, trimers lack axisymmetry, allowing us to observe rotations about all three axes and measure all six elements. In Fig. 3, we show the axis autocorrelations  $\langle \mathbf{u}_i \cdot \mathbf{u}_i(t + \tau) \rangle$  computed from 20,000 holograms, as well as best fits to exponential decays. The autocorrelation of axis 3 decays more rapidly than

TABLE I. Measured diffusion tensor elements for dimer in Fig. 2, along with analytical calculations from an exact Stokes solution [3] and numerical calculations from HYDROSUB [32]. Calculations use a best-fit particle radius  $a_{\text{eff}} = 709$  nm and solvent viscosity  $\eta_{\text{eff}} = 1.159$  mPa.s.

	Experiment	Exact	HYDROSUB
$D_{r,\perp}$ ( $\text{s}^{-1}$ )	$0.1034 \pm 0.0006$	0.1034	0.104
$D_{\parallel}$ ( $\times 10^{-13} \text{ m}^2\text{s}^{-1}$ )	$2.015 \pm 0.012$	2.010	2.02
$D_{\perp}$ ( $\times 10^{-13} \text{ m}^2\text{s}^{-1}$ )	$1.785 \pm 0.007$	1.790	1.80
$D_{\parallel}/D_{\perp}$	$1.129 \pm 0.011$	1.123	1.12

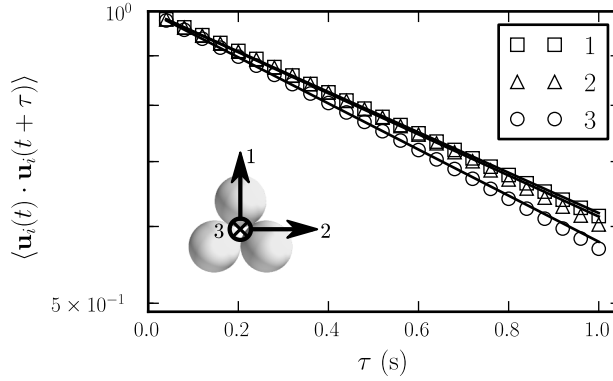


FIG. 3. Cluster axis autocorrelations  $\langle \mathbf{u}_i(t) \cdot \mathbf{u}_i(t + \tau) \rangle$  for a trimer of  $1\text{-}\mu\text{m}$  diameter spheres, showing anisotropic rotational diffusion. Open symbols are experimental measurements; error bars are comparable to or smaller than symbols. Solid lines are fits to exponential decays. Inset shows cluster axis orientation.

the autocorrelations of axes 1 and 2, in agreement with expectations: as shown in Eq. 3,  $\langle \mathbf{u}_3(t) \cdot \mathbf{u}_3(t + \tau) \rangle$  depends on  $D_{r,1}$  and  $D_{r,2}$ , both of which should be larger than  $D_{r,3}$  due to hydrodynamics. The elements of the diffusion tensor that we extract from this data are shown in Table II. The difference between  $D_{r,3}$  and both  $D_{r,1}$  and  $D_{r,2}$  is much larger than the experimental uncertainty, showing clear evidence for anisotropic rotational diffusion. The translational diffusion we observe is similarly anisotropic (Fig. 4 and Table II).

Interestingly, although our measurements of the dimensionless ratios  $D_{r,1}/D_{r,3}$  and  $D_{t,1}/D_{t,3}$  agree well with the HYDROSUB predictions, we observe small but statistically significant differences between the elements of  $\mathbf{D}$  corresponding to the two in-plane axes 1

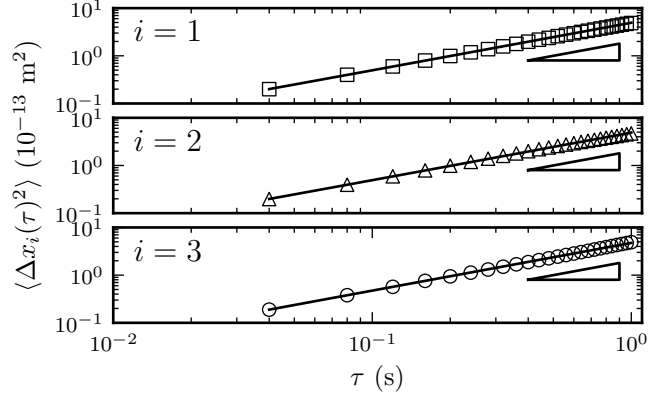


FIG. 4. Body-frame MSDs for the same trimer in Fig. 3. See inset in Fig. 3 for axis orientations  $i$ . Open symbols are experimental measurements; error bars are comparable to or smaller than symbols. Solid lines are linear fits. Triangles show MSD slope of 1.

and 2. If the particles in the trimer are identical, the threefold symmetry axis of the trimer ensures that  $D_{t,1} = D_{t,2}$  and  $D_{r,1} = D_{r,2}$  [37]. Thus the differences between these elements of the tensor imply that the particles in our trimer are not in fact identical. We performed HYDROSUB calculations to confirm that weakly breaking threefold symmetry results in differences between the in-plane elements of  $\mathbf{D}$ . Our measured ratio  $D_{r,1}/D_{r,2} = 1.03 \pm 0.02$  corresponds to a 3% size difference between the spheres. This is consistent both with the particle manufacturer's certificate of analysis as well as with particle size differences determined from holograms. This shows that the measurements are precise enough to detect the weak breaking of threefold rotational symmetry due to particle polydispersity.

Our work demonstrates experimentally how both large and small differences in the symmetry of small particles affect the diffusion tensor. The technique we use, holographic microscopy, can measure elements of the diffusion tensor to high precision, 1% or better, small enough to resolve weak symmetry breaking due to particle polydispersity. The high precision is enabled by the inherently short acquisition times of the technique, which allow us to observe rapidly diffusing systems on time scales ranging from a fraction of a rotational diffusion time  $1/D_{r,i}$  to hundreds. Although here we have measured the diffusion of isolated clusters, it should be possible to use the same technique to measure diffusion tensors in environments that are relevant to self-assembly but challenging for computation. In particular, it may be possible to measure diffusion tensors near boundaries or other particles, or for clusters that have internal degrees of freedom. There are only a few studies examining



TABLE II. Measured diffusion tensor elements for trimer shown in Figs. 3 and 4 with comparisons to computations from HYDROSUB [32]. Computations use  $a = 500$  nm obtained optically from the best-fit hologram models and  $\eta = 1.049$  mPa s from single-particle diffusion data; the difference in  $\eta$  from the dimer measurements is due to a difference in room temperature.

	Experiment	HYDROSUB
$D_{r,1}$ ( $\text{s}^{-1}$ )	$0.278 \pm 0.002$	0.296
$D_{r,2}$ ( $\text{s}^{-1}$ )	$0.270 \pm 0.002$	0.296
$D_{r,3}$ ( $\text{s}^{-1}$ )	$0.210 \pm 0.002$	0.220
$D_{r,1}/D_{r,3}$	$1.32 \pm 0.02$	1.34
$D_{r,1}/D_{r,2}$	$1.03 \pm 0.02$	1.00
$D_{t,1}$ ( $\times 10^{-13} \text{ m}^2\text{s}^{-1}$ )	$2.466 \pm 0.015$	2.64
$D_{t,2}$ ( $\times 10^{-13} \text{ m}^2\text{s}^{-1}$ )	$2.446 \pm 0.015$	2.64
$D_{t,3}$ ( $\times 10^{-13} \text{ m}^2\text{s}^{-1}$ )	$2.372 \pm 0.015$	2.41
$D_{t,1}/D_{t,3}$	$1.04 \pm 0.01$	1.09

the effect of interparticle hydrodynamic couplings on particle diffusion, and these have been restricted to spheres in planar geometries [38, 39]. Furthermore, measurements on other, even less symmetric clusters may be able to reveal translational-rotational coupling as well as the off-diagonal rotational and translational elements in the diffusion tensor.

We thank José García de la Torre, Daniela J. Kraft, Thomas G. Dimiduk, and Rebecca W. Perry for helpful discussions. This work was supported by the National Science Foundation through CAREER grant no. CBET-0747625 and through the Harvard MRSEC, grant no. DMR-0820484.

---

\* vnm@seas.harvard.edu

- [1] M. Holmes-Cerfon, S. J. Gortler, and M. P. Brenner, Proc. Nat. Acad. Sci. USA **110**, E5 (2013).
- [2] F. Perrin, J. Phys. Radium **5**, 497 (1934).
- [3] A. Nir and A. Acrivos, J. Fluid Mech. **59**, 209 (1973).

- [4] J. García de la Torre, G. del Rio Echenique, and A. Ortega, *J. Phys. Chem. B* **111**, 955 (2007).
- [5] P. Pakdel and S. Kim, *J. Rheol.* **35**, 797 (1991).
- [6] S. A. Allison, *Macromolecules* **32**, 5304 (1999).
- [7] S. Aragon and D. K. Hahn, *Biophys. J.* **91**, 1591 (2006).
- [8] M. Hoffmann, C. S. Wagner, L. Harnau, and A. Wittemann, *ACS Nano* **3**, 3326 (2009).
- [9] Y. Han, A. M. Alsayed, M. Nobili, J. Zhang, T. C. Lubensky, and A. G. Yodh, *Science* **314**, 626 (2006).
- [10] Y. Han, A. Alsayed, M. Nobili, and A. G. Yodh, *Phys. Rev. E* **80**, 011403 (2009).
- [11] S. M. Anthony, M. Kim, and S. Granick, *J. Chem. Phys.* **129**, 244701 (2008).
- [12] M. Speidel, A. Jonáš, and E.-L. Florin, *Opt. Lett.* **28**, 69 (2003).
- [13] Z. Zhang and C.-H. Menq, *Appl. Opt.* **47**, 2361 (2008).
- [14] R. Colin, M. Yan, L. Chevry, J.-F. Berret, and B. Abou, *Europhys. Lett.* **97**, 30008 (2012).
- [15] D. Mukhija and M. J. Solomon, *J. Colloid Interface Sci.* **314**, 98 (2007).
- [16] G. L. Hunter, K. V. Edmond, M. T. Elsesser, and E. R. Weeks, *Opt. Express* **19**, 17189 (2011).
- [17] R. W. Perry, G. Meng, T. G. Dimiduk, J. Fung, and V. N. Manoharan, *Faraday Discuss.* **159**, 211 (2012).
- [18] S.-H. Lee, Y. Roichman, G.-R. Yi, S.-H. Kim, S.-M. Yang, A. van Blaaderen, P. van Oostrum, and D. G. Grier, *Opt. Express* **15**, 18275 (2007).
- [19] J. Fung, K. E. Martin, R. W. Perry, D. M. Kaz, R. McGorty, and V. N. Manoharan, *Opt. Express* **19**, 8051 (2011).
- [20] J. Fung, R. W. Perry, T. G. Dimiduk, and V. N. Manoharan, *J. Quant. Spectrosc. Radiat. Transfer* **113**, 2482 (2012).
- [21] T. M. Kreis, *Opt. Eng.* **41**, 1829 (2002).
- [22] H. Brenner, *J. Colloid Interface Sci.* **23**, 407 (1967).
- [23] S. Harvey and J. García de la Torre, *Macromolecules* **13**, 960 (1980).
- [24] Eq. 1 strictly applies only for short  $\tau$  because it assumes small changes in the generalized particle probability density arising from diffusion for short  $\tau$  [22].
- [25] A. M. Yake, R. A. Panella, C. E. Snyder, and D. Velegol, *Langmuir* **22**, 9135 (2006).
- [26] L. P. Faucheux and A. J. Libchaber, *Phys. Rev. E* **49**, 5158 (1994).

- [27] D. W. Mackowski and M. I. Mishchenko, J. Opt. Soc. Amer. A **13**, 2266 (1996).
- [28] See Supplementary Information for further details.
- [29] L. D. Favro, Phys. Rev. **119**, 53 (1960).
- [30] M. Doi and S. F. Edwards, *The Theory of Polymer Dynamics* (Clarendon, Oxford, 1986).
- [31] F. C. Cheong and D. G. Grier, Opt. Express **18**, 6555 (2010).
- [32] J. García de la Torre and B. Carrasco, Biopolymers **63**, 163 (2002).
- [33] H. Flyvbjerg and H. G. Petersen, J. Chem. Phys. **91**, 461 (1989).
- [34] J. E. Seebergh and J. C. Berg, Colloids Surf., A **100**, 139 (1995).
- [35] M. R. Gittings and D. A. Saville, Colloids Surf., A **141**, 111 (1998).
- [36] J. R. Happel and H. Brenner, *Low Reynolds Number Hydrodynamics* (Kluwer, Dordrecht, 1991).
- [37] See [22, 36]. Brenner does not explicitly treat discrete rotational symmetry, but his symmetry arguments are readily applied to this case.
- [38] J. W. Merrill, S. K. Sainis, J. Bławdziewicz, and E. R. Dufresne, Soft Matter **6**, 2187 (2010).
- [39] P. P. Lele, J. W. Swan, J. F. Brady, N. J. Wagner, and E. M. Furst, Soft Matter **7**, 6844 (2011).
- [40] In terms of the diffusion tensor  $\mathbf{D}$ , for a sphere  $\mathbf{D}$  is diagonal, and  $\mathbf{D}^{tt} = D\mathbf{I}$ , where  $\mathbf{I}$  is the identity tensor.
- [41] B. J. Berne and R. Pecora, *Dynamic Light Scattering: With Applications to Chemistry, Biology, and Physics* (Wiley, 1976).
- [42] Displacements of the 3 orientational generalized coordinates  $q^i$  in Brenner’s formalism cannot describe non-infinitesimal rotations. To describe finite rotations, it is necessary to adopt a formalism such as Euler angles; see Sec. IX of Brenner’s paper for details. The general case may also be handled by coordinate-free operator methods [29].

## Supplementary Information

### Hologram Analysis and Data Reduction

We describe in further detail how we fit scattering models to the holograms we record of dimers and trimers to extract 3D dynamical information, with attention to issues that arise

with the large number of holograms ( $\sim 20,000$ ) we must analyze for each case.

### **Model Fitting Procedure**

Our technique of fitting scattering solutions to holograms has previously been described [19, 20]. For the dimers, we fit a scattering model that depends on one refractive index for both particles, the radius of each particle, the 3D position of the dimer center of mass, 2 orientational Euler angles, and a scaling parameter [19]. The model for trimers differs only in that we fit for three orientation angles and for only one average radius [20].

The largest bottleneck in fitting scattering models to large numbers of holograms using Levenberg-Marquardt minimizers is that an initial guess for the model parameters needs to be provided for each hologram. With time series of holograms, only one initial guess is necessary, in principle: we can use the best-fit parameters of each hologram as the initial guess for the next. We have found it effective to speed up this process by doing an initial rough fit to a randomly chosen subset of 10% of the pixels of each hologram. Subsequently, we use the parameters obtained from the rough fits as initial guesses for a fit to all the pixels. We do this second stage of fitting in parallel.

### **Validating Model Fits to Trimer Holograms**

The model for the trimer holograms has an additional orientational degree of freedom compared to the model for the dimer holograms. We have noticed that on occasion the fit converges to best-fit parameters that result in the best-fit model hologram having subtle differences when compared to the experimental hologram; this usually stems from the orientation angles being incorrect. We do not observe this problem for the dimer holograms. To detect holograms with potentially incorrect best-fit parameters, we inspect the  $R^2$  statistic [20] of the fits. We also compute a  $\chi^2$  statistic for a binary version of the experimental and best-fit holograms, where all pixels above the mean of 1 are set to a value of 1 and all remaining pixels are set to a value of 0. The binary image is much more sensitive to the shape of the interference fringes.

When we compute correlation functions such as mean-squared displacements from the trimer holograms, we reject the contribution from any holograms where either  $R^2$  or binary

$\chi^2$  is worse than 2 standard deviations from a rolling mean. Manual inspection of 200 randomly chosen trimer holograms that were not rejected under these criteria revealed 7 questionable fits. We infer from the Poisson distribution that, to a 99% confidence level, the percentage of remaining bad fits is less than 8%. We also reject the contribution from a given pair of holograms if the probability of obtaining either a center of mass displacement or angular displacement of the observed magnitude is less than  $10^{-5}$ . We compute these probabilities using estimates for the diffusion tensor elements, and choose the threshold of  $10^{-5}$  to avoid biasing the observed distribution and to make the cutoffs weakly sensitive to the estimates for  $\mathbf{D}$ .

Performing this cutoff procedure requires knowing the probability distributions governing translational and rotational displacements. The probability distribution for translational displacements is Gaussian, but the distribution function for rotational displacements is not. Instead, the probability density function  $f_i(\theta; \tau)$  for observing an angle  $\theta$  between cluster axis  $\mathbf{u}_i(t)$  at a given time  $t$  and after a time interval  $\tau$  is given by

$$f_i(\theta; \tau) = \sum_{\ell=0}^{\infty} Y_{\ell}^0(0) Y_{\ell}^0(\theta) \exp \left[ \frac{-\tau}{D_{r,\text{eff}} \ell(\ell+1)} \right] \quad (5)$$

where  $D_{r,\text{eff}} = (D_{r,j} + D_{r,k})/2$ ,  $D_{r,j}$  and  $D_{r,k}$  are the elements of  $\mathbf{D}^{rr}$  describing rotations about the two cluster axes other than  $i$ , and  $Y_{\ell}^0(\theta)$  denote spherical harmonics with  $m = 0$ . We briefly discuss the origin of this distribution function in Section .

As a final verification that our holographic imaging is correct and that any remaining errors do not substantially affect the dynamics we measure, we compute probability distribution functions for the dynamical quantities we use to measure  $\mathbf{D}$  from the data. Figure 5 shows a representative sample for several lag times  $\tau$ . We first examine the cosine of the angle traversed by  $\mathbf{u}_3$ , or  $\mathbf{u}_3(t) \cdot \mathbf{u}_3(t + \tau)$ , in Figure 5(a). Aside from a noise floor, we find that the measured distributions agree well with the expected distribution computed from Eq. 5 and the measured values of  $\mathbf{D}^{rr}$ . We observe similarly good agreement for the distribution of particle-frame displacements along axis 3 shown in Figure 5(b).

### Estimating Solvent Viscosities

Here we discuss in greater detail the inference of the solvent viscosities  $\eta$  needed to compare experimentally measured elements of the diffusion tensor  $\mathbf{D}$  to theoretical predictions.

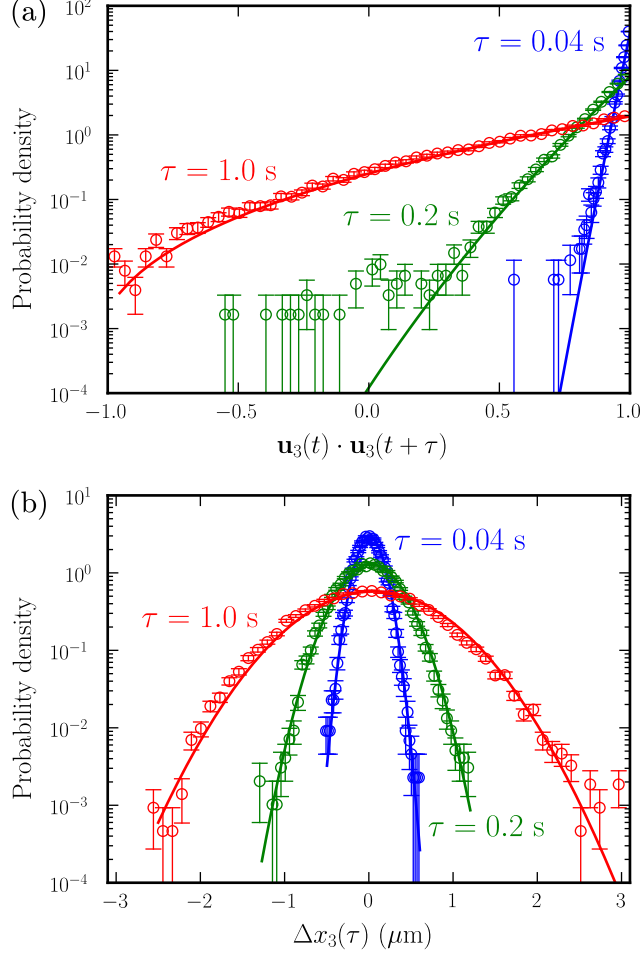


FIG. 5. Distribution functions for trimer angular displacements and cluster-frame displacements. Histogram points computed from experimental data are shown in open symbols; solid lines show theoretical predictions computed from elements of  $\mathbf{D}$  reported in Table II of the body of the paper. (a) Rotational dynamics of  $\mathbf{u}_3$ . Predicted distribution computed from Eq. 5. (b) Cluster-frame displacements along axis 3. Theoretical distribution is a Gaussian with a mean of 0 and a variance of  $2D_{t,3}\tau$ .

The viscosity of our solvent, a mixture of  $\text{H}_2\text{O}$  and  $\text{D}_2\text{O}$  chosen to density-match polystyrene particles, has a strong temperature dependence. Figure 6 shows that the viscosity of a bulk sample of the solvent, measured using a Cannon-Manning capillary viscometer, varies by nearly 20% over a  $6^\circ\text{C}$  temperature range. We performed all the experiments described in the body of the paper at room temperature, but we have observed that the room temperature can change by several  $^\circ\text{C}$  over the course of a few hours, most

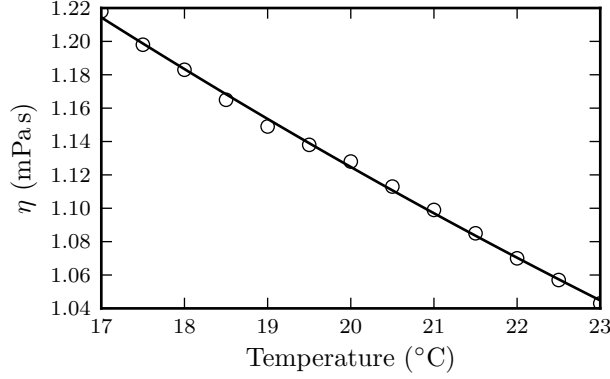


FIG. 6. Temperature dependence of solvent viscosity. Data points, open symbols, were measured with a Cannon-Manning capillary viscometer. The solid line is a best-fit quadratic function that allows for interpolation between the measured points.

likely due to the cycling of the building heating and air conditioning systems. Moreover, particularly if the laboratory room temperature is changing, the temperature in the sample, sealed in a glass sample cell, may differ from that of the surrounding air.

Consequently, we believe that the best way to estimate the solvent viscosity is to observe the *in situ* diffusion of single colloidal spheres, which are always present in the sample due to the arrested aggregation technique we use to make the clusters, either immediately before or immediately after imaging the diffusion of a cluster of interest. The Stokes-Einstein relation gives the translational diffusion constant[40]  $D$  in terms of the temperature  $T$ , the particle radius  $a$ , and the solvent viscosity  $\eta$ :

$$D = \frac{k_B T}{6\pi\eta a}. \quad (6)$$

Using Eq. 6, once we determine  $D$  for a diffusing sphere of radius  $a$ , we can infer the ratio  $k_B T/\eta$ . Because of the strong temperature dependence illustrated in Figure 6,  $k_B T$  and  $\eta$  should not be viewed as independent parameters. Moreover, from dimensional considerations, the elements of  $\mathbf{D}$  are always proportional to  $k_B T/\eta$ . Once we determine  $k_B T/\eta$ , we use the best-fit line to the data in Figure 6 to infer  $\eta$  and  $k_B T$  separately. While this is not the usual context in which microrheological experiments are performed, we essentially treat the diffusing single spheres as *in situ* thermometers.

We obtain  $D$  from an MSD computed from the 3D trajectory of a diffusing particle:  $\langle \Delta \mathbf{r}^2(\tau) \rangle = 6D\tau$ . In all cases, we obtain the trajectory using DHM and record holograms at

25 frames per second. We obtain a radius, index of refraction, and 3D position from each hologram by fitting a model based on the Lorenz-Mie solution [18].

For the dimer experiment, which used particles with a nominal radius of 650 nm, we measure  $D = 2.533 \pm 0.017 \times 10^{-13} \text{ m}^2\text{s}^{-1}$  for a diffusing particle with an optical radius of 639 nm. If we assume that the particle has the same enhanced hydrodynamic radius of 709 nm as we inferred from the dimer data, independent of any considerations of  $k_B T$  or  $\eta$ , we can subsequently use the data in Figure 6 to infer a solvent viscosity of 1.187 mPa s, which is within 3% of the best-fit solvent viscosity, 1.159 mPa s. The consistency of these values, along with the excellent agreement between the measured and predicted values of  $D_{\parallel}/D_{\perp}$ , which is independent of  $a$  and  $k_B T/\eta$ , validates our dimer measurements.

For the trimer experiment, we measured  $D = 3.996 \pm 0.055 \times 10^{-13} \text{ m}^2\text{s}^{-1}$  for a diffusing sphere of nominal radius 500 nm. With no analytical theory as we had for dimers, we cannot rigorously find a best-fit radius for the trimer. We take the optical radius of the particle, 517 nm, as an estimate of the particle size and use the data in Figure 6 to infer  $\eta = 1.049$  mPa s, the value we use in the HYDROSUB calculations.

### Probability Distribution for Rotational Displacements

We briefly describe the origin of Eq. 5, the probability density function for finite rotational displacements. As described in Section , we use this distribution to reject pairs of holograms that exhibit highly improbable angular displacements, most likely due to an incorrect model fit.

To calculate the relevant distribution function, we will consider what happens to an imaginary ensemble of clusters undergoing rotational diffusion. We will assume that translation-rotation coupling is negligible, so that we can consider the rotational motions independently of the translations. Suppose that we observe only the motion of one body axis  $\mathbf{u}_i$  as the clusters in the ensemble undergo rotational diffusion. Lastly, suppose that that we prepare the ensemble such that at  $t = 0$ ,  $\mathbf{u}_i$  for every cluster lies at the same point on the unit sphere, which we may choose to be at  $\theta = 0$  without loss of generality. We seek to compute the probability distribution  $f_i(\theta, \phi; \tau)$  such that

$$\int_{\phi_0}^{\phi_1} \int_{\theta_0}^{\theta_1} f_i(\theta, \phi; \tau) \sin \theta d\theta d\phi \quad (7)$$



gives the probability of finding  $\mathbf{u}_i$  between  $\phi_0$  and  $\phi_1$  and between  $\theta_0$  and  $\theta_1$  at  $t = \tau$ .

For isotropic rotational diffusion, such as that of a sphere, calculating  $f_i$  is straightforward: the diffusion can be described by a rotational Fick's law characterized by a single rotational diffusion constant  $D_r$  [41]. The initial condition

$$f_i(\theta, \phi; 0) = \frac{\delta(\theta)}{2\pi \sin \theta}, \quad (8)$$

where  $\delta(\theta)$  denotes the Dirac delta function, then determines  $f_i(\theta, \phi; \tau)$ . This idea can be generalized to the case we are interested in, where  $\mathbf{D}^{rr}$  is diagonal but not isotropic, using Brenner's tensorial formalism [22]. Because the details are quite involved[42], we instead give a physical argument that allows us to apply the isotropic solution to the anisotropic case.

The time evolution of  $f_i$  must be governed by  $D_{r,j}$  and  $D_{r,k}$ , the diffusion constants for rotations about the other two cluster axes. In our ensemble of clusters, prepared such that all clusters initially have  $\mathbf{u}_i$  at  $\theta = 0$ , the clusters will not all have the same orientation:  $\mathbf{u}_j$  and  $\mathbf{u}_k$  can lie anywhere on the equator of the unit sphere. Consequently, observing only the motion of  $\mathbf{u}_i$ , we will on average observe  $f_i$  evolving according to an effective rotational diffusion constant  $D_{r,\text{eff}}$  where  $D_{r,\text{eff}} = (D_{r,j} + D_{r,k})/2$ . We may then straightforwardly adopt the result from isotropic diffusion [41], which leads to Eq. 5. Note that  $f_i$  is ultimately independent of  $\phi$  because of the symmetric manner in which we prepared the ensemble.